

Numerical Study of Baroclinic Tides in Luzon Strait

SEN JAN^{1*}, REN-CHIEH LIEN² and CHI-HUA TING¹

¹*Institute of Hydrological and Oceanic Sciences, National Central University,
300 Jung-da Road, Jung-li 32001, Taiwan, R.O.C.*

²*Applied Physics Laboratory, University of Washington,
1013 NE 40th Street, Box 355640, Seattle, WA 98105-6698, U.S.A.*

(Received 29 November 2007; in revised form 20 March 2008; accepted 22 March 2008)

The spatial and temporal variations of baroclinic tides in the Luzon Strait (LS) are investigated using a three-dimensional tide model driven by four principal constituents, O_1 , K_1 , M_2 and S_2 , individually or together with seasonal mean summer or winter stratifications as the initial field. Barotropic tides propagate predominantly westward from the Pacific Ocean, impinge on two prominent north-south running submarine ridges in LS, and generate strong baroclinic tides propagating into both the South China Sea (SCS) and the Pacific Ocean. Strong baroclinic tides, ~19 GW for diurnal tides and ~11 GW for semidiurnal tides, are excited on both the east ridge (70%) and the west ridge (30%). The barotropic to baroclinic energy conversion rate reaches 30% for diurnal tides and ~20% for semidiurnal tides. Diurnal (O_1 and K_1) and semidiurnal (M_2) baroclinic tides have a comparable depth-integrated energy flux 10–20 kW m⁻¹ emanating from the LS into the SCS and the Pacific basin. The spring-neap averaged, meridionally integrated baroclinic tidal energy flux is ~7 GW into the SCS and ~6 GW into the Pacific Ocean, representing one of the strongest baroclinic tidal energy flux regimes in the World Ocean. About 18 GW of baroclinic tidal energy, ~50% of that generated in the LS, is lost locally, which is more than five times that estimated in the vicinity of the Hawaiian ridge. The strong westward-propagating semidiurnal baroclinic tidal energy flux is likely the energy source for the large-amplitude nonlinear internal waves found in the SCS. The baroclinic tidal energy generation, energy fluxes, and energy dissipation rates in the spring tide are about five times those in the neap tide; while there is no significant seasonal variation of energetics, but the propagation speed of baroclinic tide is about 10% faster in summer than in winter. Within the LS, the average turbulence kinetic energy dissipation rate is $O(10^{-7})$ W kg⁻¹ and the turbulence diffusivity is $O(10^{-3})$ m²s⁻¹, a factor of 100 greater than those in the typical open ocean. This strong turbulence mixing induced by the baroclinic tidal energy dissipation exists in the main path of the Kuroshio and is important in mixing the Pacific Ocean, Kuroshio, and the SCS waters.

Keywords:

- Numerical model,
- baroclinic tides,
- seasonal,
- fortnightly,
- Luzon Strait.

1. Introduction

Luzon Strait (LS) is the primary deep passage connecting the world's largest marginal sea, the South China Sea (SCS), to the northwest Pacific Ocean (Fig. 1(a)). Two prominent submarine ridges running north-south exist in the LS with complex and abruptly changing topography (Fig. 1(b)). The east ridge, the Luzon Island Arc, consists of a series of isles extending from the south-east coast of Taiwan to the north of Luzon. The west ridge,

the Heng-Chun Ridge, extends from the southern tip of Taiwan to the middle reaches of the LS. The east ridge is generally higher and longer than the west ridge.

The Kuroshio and tides are the dominant currents in the LS. The northward-flowing Kuroshio (Fig. 1(a)) sometimes penetrates into the LS at a speed of ~1 m s⁻¹ with a strong seasonal variation (e.g., Metzger and Hurlbert, 1996; Hu *et al.*, 2000; Centurioni *et al.*, 2004; Tian *et al.*, 2006). Massive westward intrusion of the Kuroshio occurs mostly during October to January (Centurioni *et al.*, 2004). Occasionally, anticyclonic rings detached from the Kuroshio flowing across the LS are observed in the northern SCS (Li *et al.*, 1998). The transport of the Kuroshio

* Corresponding author. E-mail: senjan@ncu.edu.tw

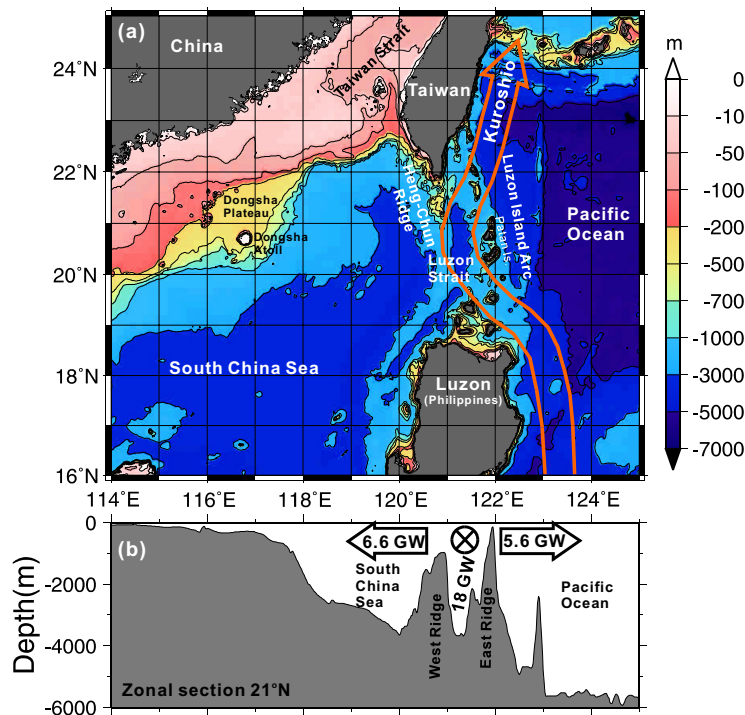


Fig. 1. (a) Bathymetry in the northern South China Sea, northwest Pacific Ocean and Luzon Strait. (b) Topographic transect along 21°N and main results of baroclinic tidal energy fluxes and dissipation. Arrows of 6.6 and 5.6 GW represent the spring-neap mean baroclinic energy fluxes that propagate into the South China Sea and the Pacific Ocean, respectively, from the Luzon Strait. About 18 GW of the baroclinic tide dissipation occurs in the Luzon Strait. ⊗ marks the Kuroshio.

into the SCS is complicated due to the fluctuation of the Kuroshio path. The Kuroshio front in the LS separates the Pacific Ocean and the SCS waters. The mixing of these two water masses depends on the available turbulent processes in the LS. Baroclinic tidal energy generated and dissipated in the LS could be one of the primary turbulence energy sources, as concluded in the present analysis.

Numerical simulations suggest that both diurnal and semidiurnal barotropic tidal currents oscillate at amplitudes of $0.05\text{--}0.3\text{ m s}^{-1}$ with major axes nearly perpendicular to the two ridges in the LS (Fang *et al.*, 1999; Jan *et al.*, 2002). The tidal sea level amplitudes of the O_1 , K_1 and M_2 are 0.25, 0.25 and 0.38 m, respectively, measured by a coastal tide gauge at southernmost Taiwan (Jan *et al.*, 2004), suggesting a nearly equal contribution of the three tidal constituents in the LS. The equal importance of the three constituents is closely related to the quasi-resonant response of the diurnal tide in the SCS (Yanagi and Takao, 1998).

Strong baroclinic tides and nonlinear internal waves with vertical isotherm displacement up to 150 m have been observed in the LS and the northern SCS near Dongsha Island (Duda *et al.*, 2004; Ramp *et al.*, 2004; Yang *et al.*, 2004). The barotropic tidal current and topography inter-

action in the LS is considered to be the major generating mechanism for the baroclinic tides (Chao *et al.*, 2007). When baroclinic tides propagate onto a shallow continental slope/shelf, the nonlinear destabilizing effect may steepen and transform baroclinic tides to nonlinear internal waves, which may be further disintegrated into a sequence of solitary waves (Gerkema and Zimmerman, 1995; Lien *et al.*, 2005). Thus the generation of baroclinic tides and the evolution from baroclinic tides to nonlinear internal waves are the focus of contemporary research using in-situ and remote-sensing observations and numerical models (Lien *et al.*, 2005; Zhao and Alford, 2006; Chang *et al.*, 2006). Niwa and Hibiya (2004) used a three-dimensional model to study M_2 baroclinic tides in the western Pacific Ocean. They concluded that 14 GW of the 54 GW westward-propagating M_2 barotropic tidal energy is converted to baroclinic tide in the LS. Nearly 7 GW (50%) of M_2 baroclinic tidal energy dissipates locally and ~ 7.4 GW (50%) propagates into SCS (4.2 GW) and into Pacific Ocean (3.2 GW). Jan *et al.* (2007) studied the effect of the K_1 baroclinic tide generated in the LS on the partial-standing, quasi-resonant barotropic tide in the SCS. The energy of the barotropic K_1 tide in the SCS is significantly reduced due to the barotropic to baroclinic energy conversion in the LS which amounts

Table 1. Parameters for calculating the adjusted height of equilibrium tides.

Constituent	Amplitude (m) of equilibrium tide (ξ)	Elasticity factor ($\alpha = 1 + k - h$)	$a (= \alpha \xi)$ for calculating H_c in (2)
O ₁	0.101	0.695	0.070
K ₁	0.142	0.736	0.105
M ₂	0.244	0.693	0.169
S ₂	0.114	0.693	0.079

up to 30% of the incident barotropic tidal energy.

The properties of baroclinic tides and nonlinear internal waves in the SCS are affected by baroclinic tides generated in the LS. A better understanding of the variations of barotropic and baroclinic tidal energetics in the LS is vital to quantify the energetics of baroclinic tides and nonlinear internal waves in the SCS and to identify the turbulence energy available for mixing water masses of the Pacific Ocean and the SCS in the LS (illustrated in Fig. 1(b)). The properties of barotropic and baroclinic tides are strongly inhomogeneous in the LS due to the complicated three-dimensional features of the two submarine ridges (Fig. 1). In-situ study to understand the dynamics of barotropic and baroclinic tides within the LS is expensive and difficult, if not impossible. The present numerical model study is motivated by a wish to study the details of baroclinic tide properties within the LS and provide guidance for future observational study. Seasonal and fortnightly variations and detailed properties of the active roles of the two ridges on generating, dissipating, and mediating energy fluxes have not been discussed in previous studies (e.g., Niwa and Hibiya, 2004; Jan *et al.*, 2007; Chao *et al.*, 2007) and form the primary focus of the present model study. The importance of the west ridge in generating and dissipating baroclinic tidal energy is also evaluated.

We use a three-dimension regional tide model, the same as that used by Jan *et al.* (2007), with realistic stratifications and tidal forcing. The seasonal mean temperature and salinity profiles derived from historical conductivity-temperature-depth (CTD) data collected in the LS are used as the initial condition. Tidal sea levels of four principal constituents (O₁, K₁, M₂ and S₂) on the open boundaries are used to drive the model, individually and in combination. Note that the Kuroshio is not represented in this model study for the model constraint and for clarity in understanding the tidal dynamics in the LS. The Kuroshio exhibits strong seasonal variations within the LS. The density front associated with the Kuroshio and its migration could affect the barotropic to baroclinic energy conversion rate and energy propagation. The relative vorticity of the Kuroshio could modify or trap the baroclinic tidal energy flux (Rainville and Pinkel, 2004).

The effects of the Kuroshio on baroclinic tides are beyond the scope of the present study and should be considered in future investigations.

2. Model Description

The three-dimensional baroclinic tide model in this study is a modification of the Princeton Ocean Model described in Blumberg and Mellor (1987). The nonlinear primitive equation model with Boussinesq and hydrostatic approximations is driven by the barotropic tidal forcing. The governing equations have been delineated in Jan *et al.* (2007). The forcing term, i.e. the tidal potential in the horizontal momentum balance, is formulated as:

$$F = gD\nabla_H(\zeta - \beta\eta), \quad (1)$$

where g is the gravitational acceleration, η is sea level displacement, D is total water depth ($D = H + \eta$, H : mean water depth), ζ is adjust height of equilibrium tides, β ($=0.940$ for diurnal tides and 0.953 for semidiurnal tides) represents the loading effect due to ocean tides (Foreman *et al.*, 1993), and $\nabla_H (= (\partial/\partial x)\vec{i} + (\partial/\partial y)\vec{j})$ is the horizontal divergence. Following Pugh (1987), the adjust height of equilibrium tides is defined as

$$\zeta = f_c H_c \cos[\omega_c t + (V_0 + \mu) + m\lambda], \quad (2)$$

where f_c is nodal factor, ω_c is frequency of corresponding tidal constituent, V_0 is initial phase angle of the equilibrium tides, μ is nodal angle, $m = 1$ or 2 accounts for diurnal or semidiurnal constituents, respectively, λ is longitude, subscript c represents tidal constituent, and H_c ($=a_1 \sin 2\phi$ or $a_2 \cos^2 \phi$ for diurnal or semidiurnal tides, ϕ : latitude) is amplitude of equilibrium tides multiplied by the factor $1 + k - h$ (k and h are Love numbers due to the elastic response and the redistribution of the mass of earth). Table 1 lists a_1 and a_2 for diurnal and semidiurnal constituents, respectively.

Since the vertical acceleration is excluded in the vertical momentum equation, processes of nonhydrostatic, nonlinear internal waves, including their conversion from baroclinic tides and interactions with baroclinic tides, are

not resolved in the present model. To parameterize these unresolved processes, we add an artificial linear dissipation term to the horizontal momentum equations similar to that adopted by Niwa and Hibiya (2004). The dissipation term is defined as

$$F_{damp} = -r(\bar{U} - \langle \bar{U} \rangle), \quad (3)$$

where \bar{U} is the horizontal velocity vector in the Cartesian coordinate, $\langle \rangle$ represents depth average, r is a damping coefficient which is set to 0.2 day^{-1} as suggested by Niwa and Hibiya (2004).

The model is bounded within $99.25^\circ\text{--}135.25^\circ\text{E}$ and $2.25^\circ\text{--}43.25^\circ\text{N}$ with $(1/12)^\circ$ horizontal resolution. There are 51 uneven σ layers in the vertical with $\sigma_k = -(0, 0.002, 0.004, 0.006, 0.008, 0.01, 0.012, 0.014, 0.018, 0.022, 0.026, 0.03, 0.034, 0.037, 0.045, 0.053, 0.061, 0.069, 0.077, 0.085, 0.1, 0.116, 0.132, 0.148, 0.179, 0.211, 0.243, 0.274, 0.306, 0.337, 0.369, 0.4, 0.432, 0.464, 0.495, 0.527, 0.558, 0.59, 0.621, 0.653, 0.684, 0.716, 0.748, 0.779, 0.811, 0.842, 0.874, 0.905, 0.937, 0.968, 1)$, from $k = 1$ (surface) to 51 (bottom). The bottom topography was established using the revised ETOPO2 (<http://www.ngdc.noaa.gov/mgg/global/relief/ETOPO2/ETOPO2v2-2006/ETOPO2v2c/>) supplement with a 1-min depth archive in the region of $105^\circ\text{--}135^\circ\text{E}$ and $2.25^\circ\text{--}35^\circ\text{N}$ provided by the National Center for Ocean Research (NCOR) of Taiwan.

Figure 2 shows the initial seasonal mean temperature (T), salinity (S) and buoyancy frequency (N) profiles above 500 m depth for summer (July to September) and winter (December to February). The profiles are derived by averaging historical CTD data, provided by NCOR, collected in the vicinity of the LS. The major difference between the two seasonal mean profiles is that the pycnocline is broader and shallower in summer than in winter, $N_{\max} = 0.018 \text{ s}^{-1}$. The mixed layer is approximately 50 m and 80 m thick in summer and winter, respectively. Below 500 m, vertical profiles of T, S and N show no significant seasonal variation. Initial fields of T and S are set to be horizontally homogeneous to exclude the currents that might be generated due to the thermal wind relation.

The motionless ocean is subsequently driven by the tidal potential and prescribed tidal sea levels on all open-ocean boundaries through a forced radiation condition similar to that used by Blumberg and Kantha (1985). The tidal sea levels on the open boundaries are computed using harmonic constants compiled in a database (hereafter NAO.99) described in Matsumoto *et al.* (2000). The barotropic and baroclinic open boundary conditions, horizontal/vertical viscosity and diffusivity, and bottom stress formulations are described in Jan *et al.* (2007). Model

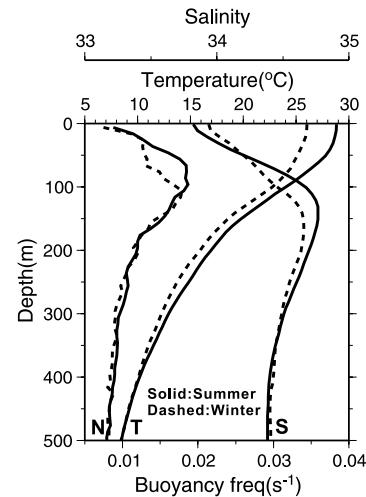


Fig. 2. Seasonal mean summer (solid lines) and winter (dashed lines) temperature, salinity and associated buoyancy frequency profiles for the initial fields of the model.

runs forced by single tidal constituent are set to 15 days; the hourly model results during the last three days, when the model reaches cyclic equilibrium, are analyzed. Model runs forced by the combined four tidal constituents, arbitrarily starting from January 1 00:00 UTC, 2006, are set to 23 days to cover the spring-neap tidal cycle. Three days of hourly model results during the spring tide (day 13~15) and neap tide (day 21~23) are analyzed to quantify the spring-neap variation.

The harmonic constants calculated from the simulated surface tides are compared with NAO.99. Figure 3 shows the model-simulated co-tidal charts for the four constituents under the summer stratification as an example. The distributions of the co-phase line for O_1 and K_1 off northern Luzon Island are likely indicative of amphidroms (Figs. 3(a) and (b)). For M_2 and S_2 , there are degenerated amphidroms north of Taiwan (Figs. 3(c) and (d)), which are consistent with those shown in Lefevre *et al.* (2000). The averaged sea level root-mean-square discrepancies for summer (winter), which considers both amplitude and phase differences, are 2.2 (2.1), 2.9 (3.1), 2.5 (2.4) and 1.0 (1.0) cm respectively for O_1 , K_1 , M_2 and S_2 as compared with the sea level calculated from NAO.99 at depths greater than 200 m in the vicinity of the LS ($115\text{--}127^\circ\text{E}$, $18\text{--}23^\circ\text{N}$). The associated goodness of fit for summer (winter) relative to the sea level calculated from NAO.99, similar to the percentage of accuracy (POA) defined in Lefevre *et al.* (2000), is 95.4 (95.4), 93.7 (93.0), 98.7 (98.8) and 98.8 (98.8)% for O_1 , K_1 , M_2 and S_2 , respectively, suggesting that barotropic tides are reasonably reproduced in the model. The difference between the harmonic constants derived from the simulated

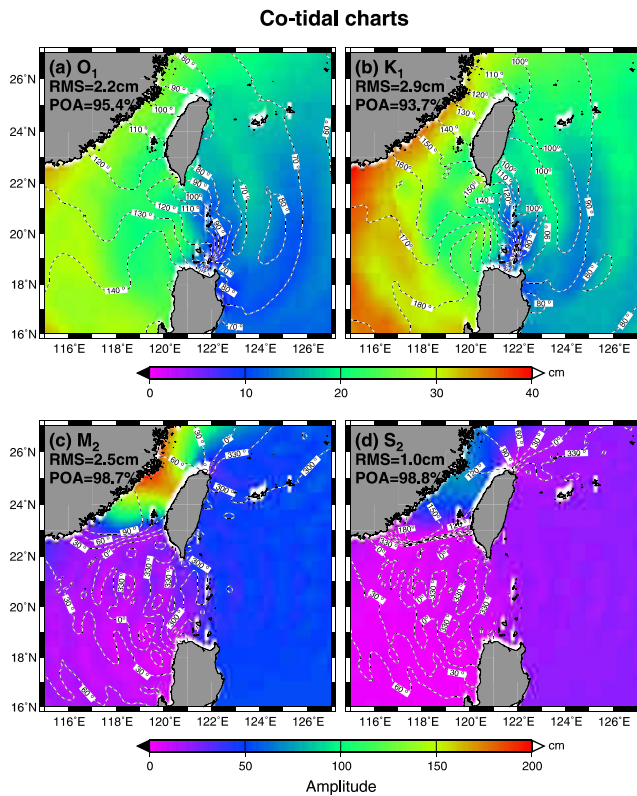


Fig. 3. Co-tidal charts for the model-simulated (a) O_1 , (b) K_1 , (c) M_2 and (d) S_2 constituents in the vicinity of the Luzon Strait. Initial field is summer stratification. Root-mean-square discrepancy (RMS) for the simulated tidal sea level relative to that calculated from NAO.99 in depths > 200 m and the associated percentage of accuracy (POA) are inserted on each panel.

surface tides in summer and winter is not significant. Further fine-tuning might improve the accuracy, but that is not the major subject of this study.

The associated depth-averaged tidal current ellipses of the four constituents are shown in Fig. 4. The characteristics of barotropic tidal currents in the LS have been delineated in many papers, e.g., Fang *et al.* (1999), Lefevre *et al.* (2000) and Niwa and Hibiya (2004), and are not repeated here. Briefly, the current amplitudes are of similar magnitude $\sim 0.2 \text{ m s}^{-1}$ for the O_1 , K_1 and M_2 and relatively small, 0.1 m s^{-1} , for the S_2 in the LS. The barotropic tidal currents are much weaker, $< 0.1 \text{ m s}^{-1}$, in the deep Pacific Ocean and the deep northern SCS. The intensification of the barotropic tidal currents in the LS is mainly due to the narrowing and shoaling topographic effects when tidal waves propagate westward from the deep western Pacific into the SCS through the two submarine ridges in the LS. The characteristic of diurnal tides, which are quasi-resonant, partial-standing waves in the SCS with a meridional nodal band roughly across the LS

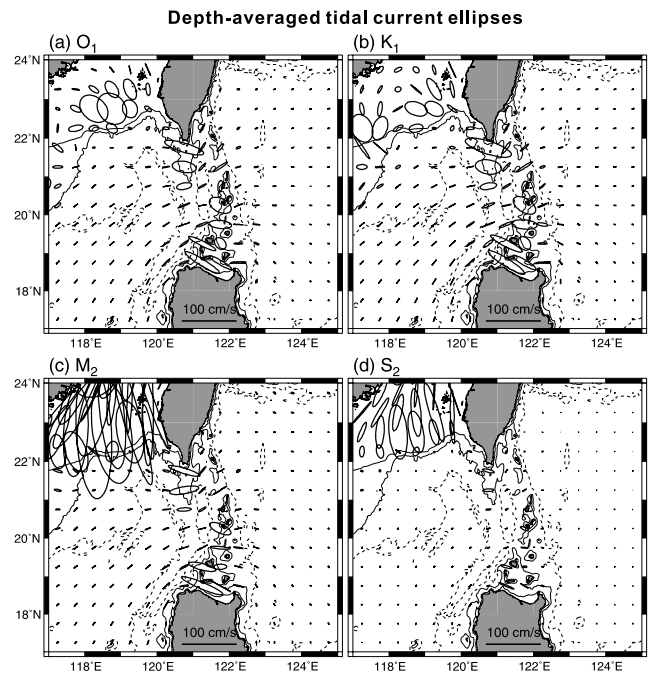


Fig. 4. Depth-averaged tidal current ellipses derived from model-simulated (a) O_1 , (b) K_1 , (c) M_2 and (d) S_2 constituents under summer stratification. 200 m (bold line), 1000 m (thin line) and 3000 m (dashed line) isobaths are appended.

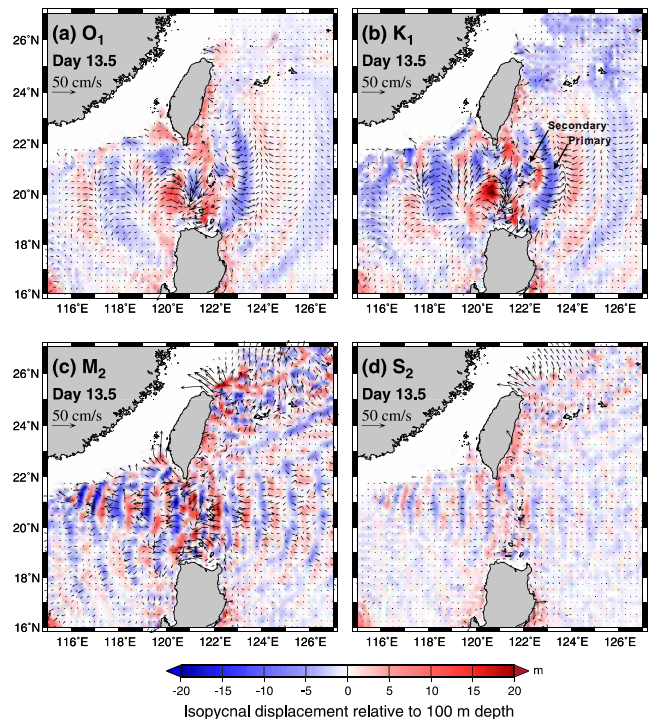


Fig. 5. Instantaneous (day 13.5) isopycnal vertical displacement relative to 100 m depth and corresponding tidal current vectors at 100 m depth derived from model results of (a) O_1 , (b) K_1 , (c) M_2 and (d) S_2 constituents under summer stratification.

(Yanagi and Takao, 1998; Jan *et al.*, 2007), also contributes to the barotropic tidal current strengthening. The major axes of tidal current ellipses of all four constituents are approximately perpendicular to the orientation of the two ridges in the LS, in favor of the generation of baroclinic tides.

It is interesting that the simulated amplitude and phase of the four tidal constituents in Fig. 3 appear to fluctuate with wavelengths similar to the horizontal wavelengths of underlying baroclinic tides around LS. Indeed, both the satellite Topex/Poseidon sea surface height and numerical results show that the strong baroclinic tides generated in the LS could modify the spatial distribution of amplitude and phase of the barotropic tide locally and even remotely in the SCS. Niwa and Hibiya (2004) attributed the short-wavelength (~ 100 km) fluctuations superposed on the simulated co-amplitude and co-phase lines (their figure 3) and along the Topex/Poseidon tracks (their figure 10) to the underlying M_2 baroclinic tides. Similar fluctuations with wavelength ~ 200 km are also found in the simulated K_1 co-tidal chart around the LS (figure 4 in Jan *et al.*, 2007).

3. Results and Discussions

3.1 General properties

Figure 5 illustrates instantaneous isopycnal vertical displacements relative to the equilibrium depth at 100 m and corresponding current velocities at day 13.5 for the four tidal constituents under the summer stratification. The amplitudes of the modeled baroclinic tides in the LS are ~ 20 m for K_1 and M_2 , ~ 10 m for O_1 , and ~ 5 m for S_2 . The complicated spatial distributions of baroclinic tidal wave patterns in the LS suggest a strong spatial inhomogeneity in the generation and propagation of baroclinic tides. The baroclinic tidal currents, as fast as 0.25 m s^{-1} , are dominant in the western Pacific Ocean and northern SCS, where the barotropic tidal currents are relatively small (cf. Fig. 4). Because of the meridional variation of the topography of the two ridges, both the zonal and meridional variations of baroclinic tidal energetics occur in the LS, which is especially clear for the diurnal tides (Figs. 5(a) and (b)). Notably, the M_2 baroclinic tides that propagate into the northern SCS have two major generating sites in the LS. One is in the northern LS, where the baroclinic tides are excited and propagate westward toward the Dongsha Island roughly along 21°N . The other is in the southern reaches of the LS, where the excited baroclinic tides propagate southwestward. These patterns are shown better below, in the form of the baroclinic tidal energy flux (Fig. 8). The two groups of baroclinic tides interfere with each other in the northern South China Sea. East of the LS, the prevailing eastward-propagating K_1 baroclinic tide is followed by a secondary wave with

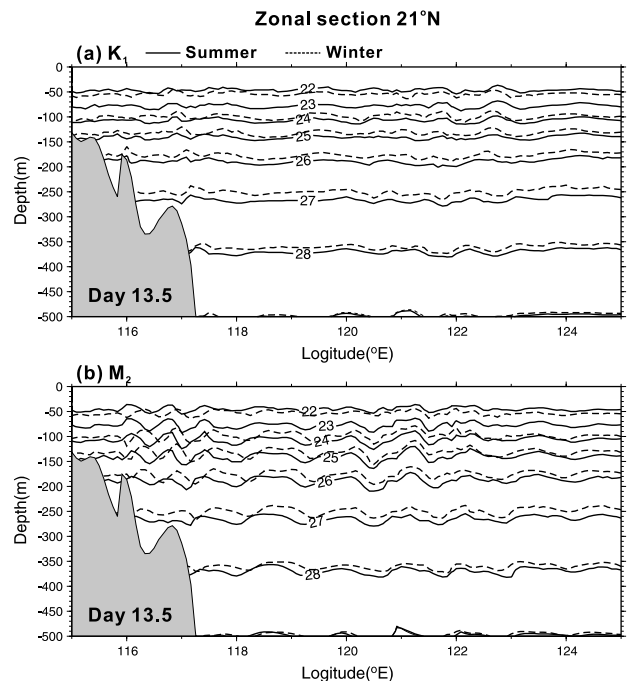


Fig. 6. Model-produced instantaneous (day 13.5) density transect along 21°N for (a) K_1 and (b) M_2 constituents under summer (solid lines) and winter (dashed lines) stratifications.

smaller amplitude, e.g., as indicated by arrows in Fig. 5(b), two successive wave troughs, separated ~ 100 km apart, at 123°E and 122°E along 21°N , respectively. Detailed analysis of the model results suggests that the former is generated at the east ridge and the latter at the west ridge. The horizontal wavelengths of diurnal and semidiurnal baroclinic tides are 300 km and 120 km, respectively, estimated subjectively from the distance between two successive prevailing wave crests (or troughs) near the LS. Near Dongsha Island, the wavelength of the semidiurnal internal tide decreases to ~ 90 km due to the shoaling of the bottom topography (Fig. 5(c)).

The model-produced isopycnal fields along 21°N , the center of the baroclinic tidal beam, for K_1 and M_2 in the two seasons are compared in Fig. 6. The seasonal difference of isopycnal fluctuations occurs mostly above 300 m depth and the westward wave propagation is slightly faster in summer than in winter. Beam-like vertical structures of baroclinic tides emanate from the two major ridges within 120.5° to 122°E and the northern SCS. The higher vertical mode is seen around the LS, especially M_2 . Propagating away from the generation site, the beam-like feature disappears quickly, suggesting the dominance of low vertical modes of baroclinic tides in the northern SCS and Pacific Ocean as high-mode baroclinic tides are dissipated. The zonal phase speed is estimated to be 2.94

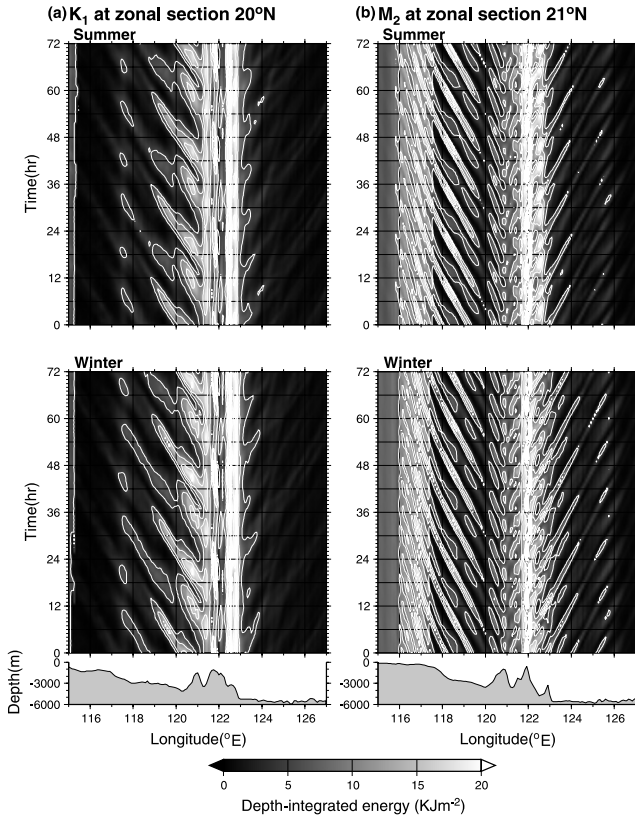


Fig. 7. Temporal and zonal variations of depth-integrated baroclinic tide energy for (a) K_1 along 20°N and (b) M_2 along 21°N in summer and winter. Relevant sectional bottom topography is inserted below. Contour interval is 2.5 kJ m^{-2} .

to 3.40 m s^{-1} for semidiurnal and diurnal constituents (Fig. 5). For the K_1 baroclinic tide, the phase speed propagating into the SCS in winter is 4% slower than that in summer, and the phase speed propagating into the Pacific Ocean in winter is 15% slower than that in summer (Fig. 5(a)). For the M_2 baroclinic tide, the zonal phase speed propagating into the SCS in winter is 14% slower than that in summer, and the phase speed propagating into the Pacific Ocean in winter is 5% slower than that in winter. Near the Dongsha Plateau, the phase speed of the M_2 baroclinic tide decreases significantly, $\sim 2 \text{ m s}^{-1}$ in summer and 1.85 m s^{-1} in winter, close to the horizontal phase speed of the first-mode internal tides: 1.96 m s^{-1} in summer and 1.8 m s^{-1} in winter. The results of the M_2 baroclinic phase speed and seasonal variations are consistent with those found by Zhao and Alford (2006).

3.2 Energy propagation

We evaluated the seasonal variations of the two dominant diurnal and semidiurnal tides. The temporal and zonal variations of the total depth-integrated baroclinic tide

Table 2. Horizontal baroclinic energy speeds estimated from Fig. 7. DS: Dongsha Plateau; SCS: northern South China Sea; PO: northwest Pacific Ocean.

Run	Stratif.	C_{gx} (m s^{-1})		
		DS	SCS	PO
K_1 at 20°N	Summer	—	2.91	2.59
	Winter	—	2.78	2.55
M_2 at 21°N	Summer	1.69	2.91	3.06
	Winter	1.56	2.84	2.91

energy for K_1 and M_2 along 20°N and 21°N are shown in Fig. 7. The two latitudes are chosen where wave crests are running nearly north-south in Figs. 5(b) and (c). The zonal component of the horizontal energy propagation speed of the baroclinic tide is computed as the averaged inverse slope of the peak energy line on Fig. 7 and is summarized in Table 2. The K_1 baroclinic energy propagates westward at $\sim 2.9 \text{ m s}^{-1}$ in summer and $\sim 2.8 \text{ m s}^{-1}$ in winter west of the LS, and propagates eastward into the Pacific Ocean at $\sim 2.6 \text{ m s}^{-1}$ in summer and winter. The M_2 baroclinic energy propagates eastward at a uniform speed, $\sim 3.0 \text{ m s}^{-1}$, from the LS to as far as 126°E . In the deep northern SCS basin, the mean zonal speed of westward-propagating M_2 baroclinic energy is $\sim 2.9 \text{ m s}^{-1}$. The westward propagation speed decreases dramatically (1.69 and 1.56 m s^{-1} in summer and winter) west of the continental slope at 118°E . Most of the M_2 baroclinic tidal energy is dissipated east of 116°E (Fig. 7(b)), which is consistent with a previous conclusion by Chang *et al.* (2006). Figure 7 also suggests the complicated baroclinic tide generation, which comprises both barotropic and baroclinic processes in the LS.

The eigen-mode speed C_1 of the first vertical mode M_2 baroclinic tides, computed using the initial vertical stratification profiles, is 2.82 m s^{-1} in summer and 2.60 m s^{-1} in winter. Alford *et al.* (2006) showed that $C_n^2 = C_g C_p$, where C_n is speed of the n -th vertical mode, C_g is the group speed, and C_p is the phase speed. For linear internal tides, $C_g = C_p(\omega^2 - f^2)\omega^{-2} \approx 0.85 C_p$ at the semidiurnal frequency. The modeled group speed is faster than the theoretical gravest mode speed and close to the phase speed. The discrepancy is probably due to the effect of nonlinearity and the superposition of eigen-modes.

When the M_2 baroclinic tide enters the shallow Dongsha Plateau, the group speed decreases to 1.69 m s^{-1} in summer and 1.56 m s^{-1} in winter. Large-amplitude nonlinear internal waves are found near Dongsha Plateau and may be converted from the shoaling internal tides (Lien *et al.*, 2005). Long-term mooring observations of nonlinear internal waves on the Dongsha Plateau show that the propagation speed of nonlinear internal waves is

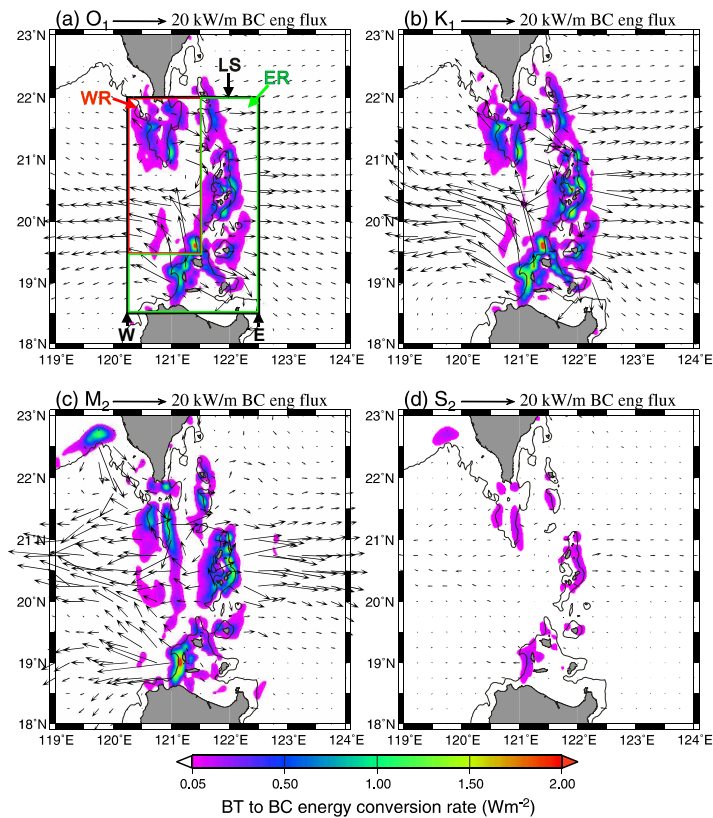


Fig. 8. Spatial distribution of depth-integrated barotropic-to-baroclinic energy conversion rate and baroclinic energy flux averaged over the last three days of simulation for (a) O_1 , (b) K_1 , (c) M_2 and (d) S_2 constituents in summer. 1000 m isobath is appended for reference.

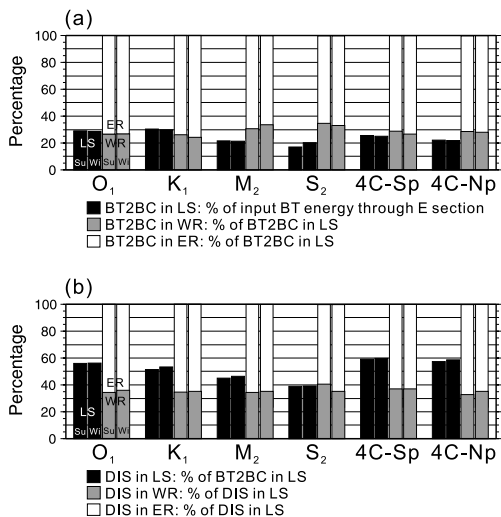


Fig. 9. (a) Percentages of barotropic-to-baroclinic conversion energy (BT2BC) in rectangular box (LS) to input barotropic energy through section E in Fig. 8 and BT2BC in the regions covering west and east ridges (WR and ER in Fig. 8) to BT2BC in LS. (b) Percentages of dissipation energy (DIS) to BT2BC in LS and DIS in regions covering WR and ER to DIS in LS.

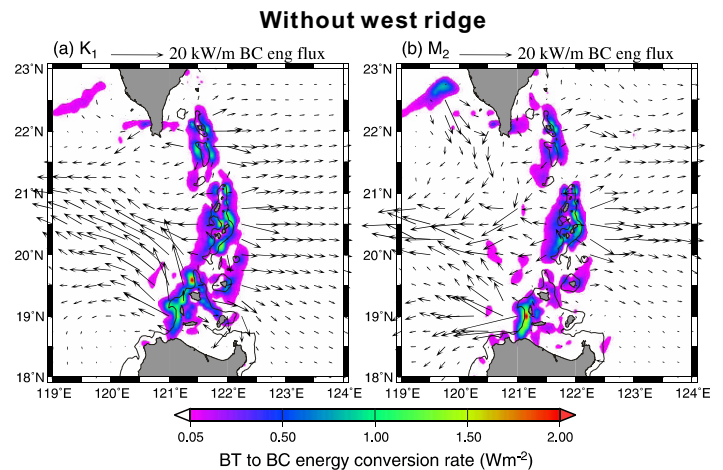


Fig. 10. As Fig. 8 but with ridge height of west ridge relative to 3000 m depth multiplied by a factor 0.1 for (a) K_1 and (b) M_2 . 1000 m isobath is appended for reference.

fastest $\sim 2 \text{ m s}^{-1}$ in the summer and slowest $\sim 1.6 \text{ m s}^{-1}$ in winter. Zhao and Alford (2006) also found the seasonal variation of M_2 baroclinic tide propagation speed, faster in summer 2.5 m s^{-1} and slower 2.2 m s^{-1} in winter, averaged between the LS and Dongsha Plateau, computed using the climatology stratification.

3.3 Energetics

The energetics of the model-produced baroclinic tides are discussed as follows. Following the formulation in Niwa and Hibiya (2004), the depth-integrated barotropic (F_{bt}) and baroclinic (F_{bc}) energy fluxes and the barotropic-to-baroclinic (bt-to-bc) energy conversion rate (E_{bt2bc}) averaged over the last three days of simulations are calculated by

$$F_{bt} = \frac{1}{T} \int_0^t \left(\langle \bar{U} \rangle \int_{-H}^{\eta} (g\rho_0(\zeta - \beta\eta) + P') dz \right) dt, \quad (4)$$

$$F_{bc} = \frac{1}{T} \int_0^t \left(\int_{-H}^{\eta} \bar{U}' P' dz \right) dt, \quad (5)$$

$$E_{bt2bc} = \frac{1}{T} \int_0^t \left(g \int_{-H}^{\eta} \rho' w_{bt} dz \right) dt, \quad (6)$$

where ρ_0 represents the initial background density stratification, \bar{U}' is the baroclinic velocity vector in the Cartesian coordinate, P' is perturbation pressure, T ($=3 \text{ d}$) is period of average, ρ' is perturbation density and

$$w_{bt} = \langle U_x \rangle \left(\sigma \frac{\partial D}{\partial x} + \frac{\partial \eta}{\partial x} \right) + \langle U_y \rangle \left(\sigma \frac{\partial D}{\partial y} + \frac{\partial \eta}{\partial y} \right) + \left(\sigma \frac{\partial \eta}{\partial t} + \frac{\partial \eta}{\partial t} \right) \quad (7)$$

is the Cartesian vertical velocity relevant to the barotropic flow. Results obtained under the summer stratification are shown in Fig. 8. The baroclinic energy of S_2 is the weakest of all constituents. Spatial distributions of the conversion rates and baroclinic energy fluxes suggest distinct effects of the east and west ridges on generating diurnal and semidiurnal baroclinic tides. Considering the barotropic tidal current and topography indicated in Fig. 4, and examining the region of high area-integrated bt-to-bc conversion rate in Fig. 8, the strong tidal current and topography interaction occurs mostly over the east ridge around the Batan Islands.

The baroclinic tidal energy fluxes of O_1 and K_1 propagate eastward into the Pacific Ocean in a tidal beam $\sim 300 \text{ km}$ wide, comparable to the meridional extent of the east ridge in the LS, centered at 20.5°N (Figs. 8(a)

and (b)). The energy conversion from the barotropic tides to the baroclinic tides occurs along the entire east ridge at a rate of $>0.05 \text{ W m}^{-2}$ along most of the ridge. The energy flux of K_1 is slightly greater than that of O_1 , with an average flux of $\sim 10 \text{ kW m}^{-1}$ immediately east of the LS. Propagating westward into the SCS from the LS, the baroclinic tidal energy fluxes of O_1 and K_1 emanate mostly from the southern end of the east ridge in a narrower (150 km) tidal beam centered at 20°N . The westward energy flux is about 15 kW m^{-1} , greater than that of the eastward energy flux; it propagates northward first between the two ridges, and then turns to the west. The meridionally integrated eastward baroclinic energy fluxes of O_1 and K_1 into the Pacific Ocean are comparable to the meridionally integrated westward energy fluxes into the SCS, with different tidal beam widths. The northern part of the west ridge is a secondary generation site ($\sim 26\%$) of diurnal baroclinic tides.

The conversion of the M_2 barotropic tide to the baroclinic tide occurs on both the east and west ridges at a rate similar to that of diurnal tide. The eastward-propagating M_2 baroclinic energy has a tight beam width of 125 km , between 20 and 21.25°N centered at 20.5°N (Fig. 8(c)). The maximum eastward energy flux into the Pacific Ocean reaches $\sim 20 \text{ kW m}^{-1}$ with an average of 10 kW m^{-1} immediately east of the LS. The M_2 baroclinic energy flux west of the LS into the SCS is generated at two primary sites, the east ridge south of 21°N and the west ridge north of 21°N . These two energy fluxes merge into a nearly 125 km tidal beam propagating westward. A sizable fraction of the baroclinic energy that emanated from the southern part of east ridge propagates southwestward centered at 19°N (Fig. 8(c)).

The modeled baroclinic tidal energy flux in the LS is nearly ten times that in the deep basins at the western Pacific and near Hawaii, $1\text{--}2 \text{ kW m}^{-1}$, estimated using historical hydrographic and mooring measurements (Alford, 2003). It is comparable to the observed strong semidiurnal internal tidal energy flux, $O(10) \text{ kW m}^{-1}$, radiating from the Hawaiian Ridge (Lee *et al.*, 2006).

The energy budgets averaged over the last three days of the model simulations in the LS, i.e., the rectangular box in Fig. 8(a), for all four constituents in two seasons are analyzed and summarized in Table 3. The 3-day averaged, depth-integrated baroclinic dissipation rate is computed as the difference of the divergence of baroclinic energy flux and the bt-to-bc energy conversion rate, i.e. $\nabla \cdot F_{bc} - E_{bt2bc}$. The sectional-integrated barotropic energy in the east section ranges from approximately 27 to 45 GW ($1 \text{ GW} = 10^9 \text{ W}$) for the three major constituents, O_1 , K_1 and M_2 and exhibit little seasonal variation. Both diurnal and semidiurnal barotropic tidal energy fluxes propagate westward from the Pacific Ocean, across the LS, and into the SCS.

Table 3. Energetics in the Luzon Strait. TS: initial temperature and salinity profiles of summer (Su) or winter (Wi); Tid: tidal stage for spring (Sp) or neap (Np) tides; BTE: meridional-section integrated barotropic energy at the east (E) and west (W) sections of the rectangular box in Fig. 8; BT2BC: area-integrated barotropic-to-baroclinic energy conversion rate in the Luzon Strait (LS) and the regions over the west (WR) and east (ER) ridges; BCE: meridional-section integrated baroclinic energy at E and W sections; ~DIS: area-integrated approximately energy dissipation (divergence of the baroclinic energy flux – BT2BC) over LS, WR and ER. 4C means the four constituents composed together. Negative values of BTE and BCE mean westward. Units are GW (10^9 W). All quantities are averaged over three days of simulation.

Run	TS	Tid	BTE		BT2BC			BCE		~DIS		
			W	E	LS (%BTE-E)	WR (%LS)	ER (%LS)	W	E	LS (%BT2BC)	WR (%LS)	ER (%LS)
O ₁	Su	—	-28.43	-27.11	7.89 (29.1)	2.10 (26.6)	5.79 (73.4)	-1.56	1.73	4.41 (55.9)	1.52 (34.5)	2.89 (65.5)
	Wi	—	-28.05	-26.80	7.65 (28.5)	2.06 (26.9)	5.59 (73.1)	-1.54	1.65	4.30 (56.2)	1.55 (36.0)	2.75 (64.0)
K ₁	Su	—	-34.00	-36.92	11.24 (30.4)	2.92 (26.0)	8.32 (74.0)	-2.73	2.43	5.79 (51.5)	2.01 (34.7)	3.78 (65.3)
	Wi	—	-33.39	-37.84	11.33 (30.0)	2.74 (24.2)	8.59 (75.8)	-2.75	2.26	6.03 (53.2)	2.12 (35.2)	3.91 (64.8)
M ₂	Su	—	-32.45	-44.01	9.53 (21.7)	2.93 (30.7)	6.60 (69.3)	-3.02	2.30	4.30 (45.1)	1.48 (34.4)	2.82 (65.6)
	Wi	—	-30.51	-45.68	9.72 (21.3)	3.27 (33.6)	6.45 (66.4)	-2.88	2.03	4.50 (46.3)	1.59 (35.3)	2.91 (64.7)
S ₂	Su	—	-3.27	-7.06	1.21 (17.1)	0.42 (34.7)	0.79 (65.3)	-0.39	0.36	0.47 (38.8)	0.19 (40.4)	0.28 (59.6)
	Wi	—	-3.59	-6.40	1.30 (20.3)	0.43 (33.1)	0.87 (66.9)	-0.39	0.41	0.51 (39.2)	0.18 (35.3)	0.33 (64.7)
4C	Su	Sp	-177.32	-196.09	50.35 (25.7)	14.50 (28.8)	35.85 (71.2)	-10.73	9.28	29.75 (59.1)	11.00 (37.0)	18.75 (63.0)
	Wi	Sp	-175.28	-199.57	49.86 (25.0)	14.27 (28.6)	35.58 (71.4)	-10.40	8.99	29.77 (59.7)	11.05 (37.1)	18.72 (62.9)
	Su	Np	-42.69	-50.00	11.07 (22.1)	2.96 (26.7)	8.10 (73.3)	-2.63	2.00	6.33 (57.2)	2.07 (32.7)	4.26 (67.3)
	Wi	Np	-41.43	-50.97	11.23 (22.0)	3.16 (28.1)	8.07 (71.9)	-2.53	2.04	6.58 (58.6)	2.32 (35.3)	4.26 (64.7)

About 30% of the westward incident diurnal barotropic tidal energy converts to the baroclinic tide, and about 21% of the incident semidiurnal barotropic tidal energy converts to baroclinic tide (Fig. 9). Note that the incident barotropic tidal energy here means the zonal component of energy flux through the east section E in Fig. 8, because it is the most effective component in generating baroclinic tides over the meridional ridges. The model conversion rate for M₂ is close to the result of Niwa and Hibiya (2004). Nearly 19 GW (O₁ + K₁) and 11 GW (M₂ + S₂) of diurnal and semidiurnal baroclinic tides, respectively, are generated in the LS. About 30% is generated at the west ridge and 70% at the east ridge (Fig. 9). About 4 GW of baroclinic diurnal tides propagates into the SCS and 4 GW into the Pacific Ocean. About 3 GW of baroclinic semidiurnal tides propagates into the SCS and 3 GW into the Pacific Ocean. Nearly 50% of baroclinic tides generated in the LS is dissipated locally (Fig. 9): 10 GW for baroclinic diurnal tides and 5 GW for the baroclinic semidiurnal tides (Table 3). Compared with

the results of baroclinic tide study along the Hawaiian ridge, Klymak *et al.* (2006) found 8–25% of baroclinic tidal energy, 2–4.5 GW, is dissipated locally, and the rest propagates away. Our model result of 50% local dissipation of baroclinic tidal energy is consistent with the result of Niwa and Hibiya (2004), and is likely caused by the effect of double ridges. Baroclinic tides generated at one ridge interact with the other ridge within a short distance, <100 km, from their generation sites. The dissipated baroclinic tidal energy may be the source of the local turbulence mixing, which is potentially important for mixing water masses in the Pacific Ocean, Kuroshio, and the SCS.

The 3-day averaged, LS area-integrated barotropic tide energy calculated from the divergence of the barotropic energy flux indicates that the K₁ barotropic energy is ~-12 GW (negative means energy loss) which is balanced by the bt-to-bc energy conversion (~11 GW) and the dissipation due to friction (~1 GW). A similar estimate of M₂ indicates that ~18 GW of barotropic tide

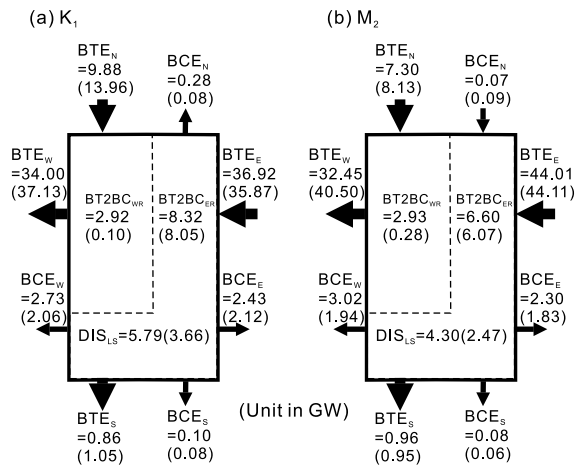


Fig. 11. Diagram showing 3-day averaged, area-integrated baroclinic energy dissipation (DIS) and barotropic-to-baroclinic conversion energy (BT2BC) over west ridge (WR) and east ridge (ER) and meridional sectional area-integrated barotropic (BT) and baroclinic (BC) tide energy through east (E), west (W), north (N) and south (S) boundaries of the LS for (a) K_1 and (b) M_2 on topography with or without the west ridge. Numbers in parentheses indicate corresponding energetics calculated from model runs without the west ridge. All quantities are GW.

energy is lost in the LS, which is balanced by ~ 10 GW of bt-to-bc conversion and ~ 8 GW of local barotropic dissipation. These estimates are schematically shown in Fig. 11 below.

3.4 Role of west ridge

Chao *et al.* (2007) identified the west ridge in the middle portion of the LS as a damper of incoming M_2 baroclinic tide from the east ridge; while in the northern portion of the LS, the west ridge becomes a secondary generation site for M_2 baroclinic tide. Based on the model results, Jan *et al.* (2007) concluded that the east ridge is the major source of K_1 baroclinic tide in the SCS. To further evaluate the effect of the west ridge in generating and dissipating baroclinic tides we conducted two additional experiments with the height of the west ridge relative to 3000 m depth reduced by 90%, i.e., deepening the west ridge artificially to ~ 3000 m, leaving all other model settings unchanged for K_1 and M_2 . Hereafter we refer to this case as “without west ridge” for convenience. Figure 10 illustrates the 3-day averaged, depth-integrated bt-to-bc conversion energy and baroclinic energy fluxes for K_1 and M_2 . If one compares Figs. 8 and 10, one sees that an unrealistic deep west ridge suppresses the generation of baroclinic tides along the northern west ridge. Without the west ridge, the spatial distribution of K_1 baroclinic energy flux east of the east ridge (Fig. 10(a)) differs little

from that with the west ridge (Fig. 8(b)); the M_2 baroclinic energy beam changes from one (Fig. 8(c)) to two separated beams (Fig. 10(b)). West of the east ridge, the spatial structure of baroclinic energy fluxes for both K_1 and M_2 differ significantly from those shown in Fig. 8. The westward-propagating K_1 beam in Fig. 8(b) is shifted 0.5° north and becomes narrower in Fig. 10(a). The west ridge apparently serves as a block, keeping the westward K_1 energy beam centered at 20.5° N. The width of the westward M_2 baroclinic tidal energy beam (Fig. 10(b)) narrows to about two thirds of that in Fig. 8(c), which implies that the west ridge is more important in generating westward propagating M_2 baroclinic tides than K_1 baroclinic tides.

Figure 11 compares the area-integrated bt-to-bc energy, sectional area-integrated baroclinic tidal energy fluxes, and dissipation of baroclinic tidal energy calculated from the model runs with and without the west ridge for K_1 and M_2 under the summer stratification. The eastward baroclinic energy through section E in Fig. 8(a) decreases to 2.12 and 1.83 GW for K_1 and M_2 without the west ridge, which corresponds to 12.7% and 20.4% reduction of that with the west ridge. Through the west section W in Fig. 8(a), the westward K_1 and M_2 baroclinic energy drops to 2.06 and 1.94 GW, corresponding to a decrease of 20.8% and 35.7% of that with the west ridge. The west ridge plays a more significant role in modulating the M_2 baroclinic tide than modulating the K_1 baroclinic tide in SCS. Without the west ridge, the area-integrated baroclinic tidal energy dissipation in the LS reduces to 36.7% (5.79 vs. 3.66 GW) and 42.5% (4.30 vs. 2.47 GW) of that with the west ridge for K_1 and M_2 baroclinic tides. The higher reduction rates of baroclinic tidal energy and dissipation for M_2 indicate that the west ridge is more efficient in generating and dissipating M_2 baroclinic tides than K_1 baroclinic tides. The reduction of the baroclinic tidal energy dissipation rate in the LS without the west ridge suggests the importance of the double ridges in the LS in dissipating baroclinic tides.

3.5 Properties of combined constituents

Model simulations of the combined four tidal constituents, which are closer to reality, are performed to compare the spring-neap variations. The depth-integrated bt-to-bc conversion rate and baroclinic energy fluxes are shown in Fig. 12. Again, there is no significant seasonal variation, but strong spring-neap variation. The westward-propagating barotropic energy entering the LS amounts to as much as 200 GW, approximately 25% of which is converted to baroclinic energy in the LS during the spring tide; the incident barotropic energy drops greatly to 11 GW, 22% of which is converted to baroclinic energy during the neap tide (Table 3). During the spring tide, over most of the west and east ridges, >0.05 $W m^{-2}$ of

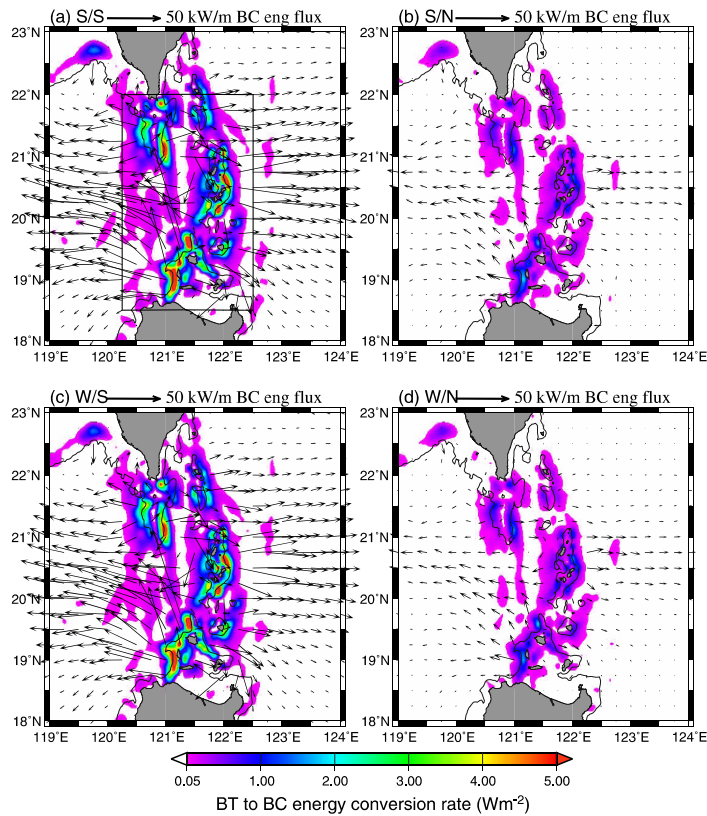


Fig. 12. As Fig. 5 but for the four constituents combined together during (a) spring (b) neap tides under summer stratification.

baroclinic tidal energy is generated, with some hot spots of $>5 \text{ W m}^{-2}$. Two nearly 300 km wide tidal beams emanate from the Luzon Strait into the SCS and the Pacific Ocean, centered at $\sim 20.5^\circ\text{N}$ with an average energy flux of $\sim 50 \text{ kW m}^{-1}$ close to the generation site.

During the spring tide, integrated over the LS, $\sim 50 \text{ GW}$ of baroclinic tidal energy is generated in a spring tide, 28% at the west ridge, $\sim 10 \text{ GW}$ propagates into the SCS, $\sim 9 \text{ GW}$ propagates into the Pacific Ocean, and $\sim 30 \text{ GW}$ is dissipated locally, 40% of it at the west ridge (see Table 3 and Fig. 9). During the neap tide, $\sim 11 \text{ GW}$ of baroclinic tidal energy is generated, $\sim 5 \text{ GW}$ propagates away, and $\sim 6 \text{ GW}$ is dissipated locally. Although the magnitudes of energetics show a factor of five in spring-neap variations, the ratios of the area-integrated bt-to-bc energy conversion rate to the incident barotropic energy, and the baroclinic dissipation to the bt-to-bc conversion rate remain nearly the same in the LS (Fig. 9). When averaged over the spring-neap cycle, the meridionally integrated baroclinic tidal energy flux is 6.6 GW into the South China Sea and 5.6 GW into the Pacific Ocean (Fig. 1(b)). Approximately 58% of baroclinic tidal energy, $\sim 18 \text{ GW}$, generated in the Luzon Strait dissipates locally. For comparison, most of baroclinic tidal energy generated in other topographic features in the ocean propagates away

and little is dissipated locally. The strong baroclinic tidal energy dissipation in the LS is more than five times that estimated in the vicinity of the Hawaiian ridge, which might be attributed to the interaction between baroclinic tides and the complicated double-ridge topography.

3.6 Turbulence dissipation

Nearly 18 GW of baroclinic tidal energy is dissipated in the LS. The turbulence kinetic energy dissipation rate per unit water mass, ε , averaged within the LS is $\sim 10^{-7} \text{ W kg}^{-1}$, a factor 100 greater than that in a typical open ocean. The vertical eddy diffusivity can be computed following the Osborn method (Osborn, 1980) as $K_\rho = 0.2\varepsilon N^{-2}$. Given the depth averaged stratification $N = 0.004 \text{ s}^{-1}$, a bulk estimate of K_ρ is $O(10^{-3}) \text{ m}^2\text{s}^{-1}$, which is 100 times that in the abyssal ocean with typical internal wave field (Toole *et al.*, 1994). The estimated vertical diffusivity is similar to that computed from the hydrographic data (Qu *et al.*, 2006).

In the close vicinity of generation sites, baroclinic tides may dissipate along the tidal beam via shear instability (Lueck and Mudge, 1997; Lien and Gregg, 2001). Lien and Gregg (2001) found $\varepsilon = O(10^{-6}) \text{ W kg}^{-1}$ and $K_\rho > 0.01 \text{ m}^2\text{s}^{-1}$ in a thin 50-m layer along the M_2 baroclinic tidal beam within 4 km from the shelf break

where baroclinic tides are generated. Although the shear instability can dissipate high-mode internal tides effectively, but it occurs only in a small fraction of the water column and dissipates only a small percentage of the total baroclinic tidal energy. For example, only 8–25% of baroclinic tides generated along the Hawaiian ridge is dissipated locally (Klymak *et al.*, 2006).

Identifying the dynamic mechanisms responsible for the strong dissipation rate (50%) of baroclinic tides generated in the LS is beyond the scope of this numerical model study. Intuitively, we expect that the complex double ridge topography, within ~100 km, interacts strongly with baroclinic tides in the LS. When baroclinic tides are generated at one ridge and propagate onto the other ridge, the shoaling topography could enhance the baroclinic tidal shear in the interior and near the bottom. Small-scale processes such as hydraulic jumps might occur over the rough topography. Baroclinic tides may become nonlinear and convert into internal solitary waves (Lien *et al.*, 2005). Lien *et al.* (2005) estimated a ~16% conversion rate from baroclinic tides to internal solitary waves on a shoaling continental slope in the northern SCS. Since internal solitary waves are not resolved in the present numerical model, the conversion into internal solitary waves is represented as the local loss of baroclinic tidal energy. All these small-scale processes could be responsible for the large dissipation rate of baroclinic tides in the LS. Further numerical models or observation campaigns are needed to understand the exact dissipation mechanisms of baroclinic tides in the LS.

4. Summary

The temporal and spatial variations of baroclinic tides in the LS have been investigated using a three-dimensional tide model driven by four principal tidal constituents, O_1 , K_1 , M_2 and S_2 . Simulations were performed with four individual constituents and with the combined tide separately, and initialized with different seasonal vertical stratifications.

The model results allow us to conclude that there is little seasonal variation in the baroclinic energy budget. The baroclinic tidal propagation speed, including group, phase, and eigen-mode speed, is about 10% greater in summer than in winter. About 20 GW of baroclinic diurnal tide and ~10 GW of baroclinic semidiurnal tide are generated in the LS, with ~30% on the west ridge and 70% on the east ridge. The semidiurnal baroclinic tide has a narrow energy beam of ~125 km compared to ~300 km for the diurnal baroclinic tide. The semidiurnal baroclinic tidal energy flux emanating westward from the east ridge and that from the northern west ridge combine to form a strong westward narrow tidal beam propagating across the SCS basin onto the Dongsha Plateau. This semidiurnal baroclinic energy flux is likely the energy

source for the large-amplitude nonlinear internal waves found in the SCS. Nearly 50% of the baroclinic tidal energy, ~18 GW on average, generated in the LS dissipates locally due to the unique double-ridge effect in the LS. This is distinctly more dissipative than baroclinic tides generated in other topographic features in the ocean, which is often <25%. The strong baroclinic tidal energy dissipation in the LS is more than five times that estimated in the vicinity of the Hawaiian ridge.

The spring-neap variation of baroclinic energy budget is significant. In the spring tide, nearly 50 GW of the combined baroclinic tidal energy is generated in the LS, 20 GW propagates away, and 30 GW dissipates locally; while in neap tide, merely 11 GW is generated, ~4.5 GW propagates away, and ~6.5 GW dissipates locally. The strong dissipation of baroclinic tidal energy may provide energy for the mixing of water masses among the Pacific Ocean, Kuroshio, and the SCS. Our results suggest that the mixing should exhibit significant spring-neap variation. Within the LS, the average turbulence kinetic energy dissipation rate ε is $O(10^{-7})$ W kg⁻¹ and the turbulence diffusivity is $O(10^{-3})$ m²s⁻¹, a factor 100 greater than those in the typical open ocean. Note that the Kuroshio is likely to play an important role in modulating the baroclinic tide's generation, trapping, dissipation, and propagation (Chao *et al.*, 2007). Excluding the Kuroshio helps clarify our model results concerning the barotropic and baroclinic energy budgets, but the model is undoubtedly as over simplification. Further investigations including the Kuroshio effect are needed.

Acknowledgements

This study is funded by Taiwan's National Science Council under grant NSC95-2611-M-008-004-MY3. R.-C. Lien is supported by Office of Naval Research of US under grant N00014-04-1-0237. The Taiwan's National Center for Ocean Research (NCOR) provided 1-min bathymetry and historical CTD data. Three anonymous reviewers contributed substantially to the improvement of this paper.

References

- Alford, M. H. (2003): Redistribution of energy available for ocean mixing by long-range propagation of internal waves. *Nature*, **423**, 159–163.
- Alford, M. H., M. C. Gregg and M. A. Merrifield (2006): Structure, propagation, and mixing of energetic baroclinic tides in Mamala Bay, Oahu, Hawaii. *J. Phys. Oceanogr.*, **36**, 997–1018.
- Blumberg, A. F. and L. H. Kantha (1985): Open boundary condition for circulation models. *J. Hydr. Eng.*, **111**(2), 237–255.
- Blumberg, A. F. and G. F. Mellor (1987): A description of a three dimensional coastal ocean circulation model. p. 1–16. In *Three-Dimensional Coastal Ocean Models*, Coastal

- and Estuarine Stud., Vol. 4, ed. by N. Heaps, AGU, Washington, D.C.
- Centurioni, L. R., P. P. Niller and D.-K. Lee (2004): Observations of inflow of Philippine Sea surface water into the South China Sea through the Luzon Strait. *J. Phys. Oceanogr.*, **34**, 113–121.
- Chang, M.-H., R.-C. Lien, T. Y. Tang, E. A. D'Asaro and Y. J. Yang (2006): Energy flux of nonlinear internal waves in northern South China Sea. *Geophys. Res. Lett.*, **33**, L03607, doi:10.1029/2005GL025196.
- Chao, S.-Y., D.-S. Ko, R.-C. Lien and P.-T. Shaw (2007): Assessing the west ridge of Luzon Strait as an internal wave mediator. *J. Oceanogr.*, **63**, 897–911.
- Duda, T. F., J. F. Lynch, J. D. Irish, R. C. Beardsley, S. R. Ramp, C.-S. Chiu, T.-Y. Tang and Y.-J. Yang (2004): Internal tide and nonlinear internal wave behavior at the continental slope in the northern South China Sea. *IEEE J. Oceanic Eng.*, **29**(4), 1105–1130.
- Fang, G., Y.-K. Kwok, K. Yu and Y. Zhu (1999): Numerical simulation of principal tidal constituents in the South China Sea, Gulf of Tonkin and Gulf of Thailand. *Cont. Shelf Res.*, **19**, 845–869.
- Foreman, M. G. G., R. F. Henry, R. A. Walters and V. A. Ballantyne (1993): A finite element model for tides and resonance along the north coast of British Columbia. *J. Geophys. Res.*, **98**, 2509–2532.
- Gerkema, T. and J. T. F. Zimmerman (1995): Generation of nonlinear internal tides and solitary waves. *J. Phys. Oceanogr.*, **25**, 1081–1094.
- Hu, J., H. Kawamura, H. Hong and Y. Qi (2000): A review on the currents in the South China Sea: seasonal circulation, South China Sea Current and Kuroshio intrusion. *J. Oceanogr.*, **56**, 607–624.
- Jan, S., C.-S. Chern and J. Wang (2002): Transition of tidal waves from the East to South China Seas over the Taiwan Strait: Influence of the abrupt step in the topography. *J. Oceanogr.*, **58**, 837–850.
- Jan, S., C.-T. A. Chen, Y.-Y. Tu and H.-S. Tsai (2004): Physical properties of thermal plumes from a nuclear power plant in the southernmost Taiwan. *J. Mar. Sci. Tech.*, **12**(5), 433–441.
- Jan, S., C.-S. Chern, J. Wang and S.-Y. Chao (2007): Generation of diurnal K_1 internal tide in the Luzon Strait and its influence on surface tide in the South China Sea. *J. Geophys. Res.*, **112**, C06019, doi:10.1029/2006JC004003.
- Klymak, J. M., J. N. Moum, J. D. Nash, E. Kunze, J. B. Girton, G. S. Carter, C. M. Lee, T. B. Sanford and M. C. Gregg (2006): An estimate of tidal energy lost to turbulence at the Hawaiian Ridge. *J. Phys. Oceanogr.*, **36**, 1148–1164.
- Lee, C. M., E. Kunze, T. B. Sanford, J. D. Nash, M. A. Merrifield and P. E. Holloway (2006): Internal tides and turbulence along the 3000-m isobath of the Hawaiian Ridge. *J. Phys. Oceanogr.*, **36**, 1165–1183.
- Lefevre, F., C. Le Provost and F. H. Lyard (2000): How can we improve a global ocean tide model at a regional scale? A test on the Yellow Sea and the East China Sea. *J. Geophys. Res.*, **105**(C4), 8707–8725.
- Li, L., W. D. Nowlin, Jr. and J. Su (1998): Anticyclonic rings from the Kuroshio in the South China Sea. *Deep-Sea Res. I*, **45**, 1469–1482.
- Lien, R. C. and M. C. Gregg (2001): Observations of turbulence in a tidal beam and across a coastal ridge. *J. Geophys. Res.*, **106**, 4575–4591.
- Lien, R.-C., T. Y. Tang, M. H. Chang and E. A. D'Asaro (2005): Energy of nonlinear internal waves in the South China Sea. *Geophys. Res. Lett.*, **32**, L05615.
- Lueck, R. G. and T. D. Mudge (1997): Topographically induced mixing around a shallow seamount. *Science*, **276**, 1831–1833.
- Matsumoto, K., T. Takanezawa and M. Ooe (2000): Ocean tide models developed by assimilating TOPEX/POSEIDON altimeter data into hydrodynamical model: a global model and a regional model around Japan. *J. Oceanogr.*, **56**, 567–581.
- Metzger, E. J. and H. E. Hurlbert (1996): Coupled dynamics of the South China Sea, the Sulu Sea, and the Pacific Ocean. *J. Geophys. Res.*, **101**, 12331–12352.
- Niwa, Y. and T. Hibiya (2004): Three-dimensional numerical simulation of M_2 internal tides in the East China Sea. *J. Geophys. Res.*, **109**, C04027, doi:10.1029/2003JC001923.
- Osborn, T. R. (1980): Estimates of the local rate of vertical diffusion from dissipation measurements. *J. Phys. Oceanogr.*, **10**, 83–89.
- Pugh, D. T. (1987): *Tides, Surges and Mean Sea-Level*. Wiley, Chichester, 471 pp.
- Qu, T., J. B. Gritton and J. A. Whitehead (2006): Deepwater overflow through Luzon Strait. *J. Geophys. Res.*, **111**, C01002, doi:10.1029/2005JC003139.
- Rainville, L. and R. Pinkel (2004): Observations of energetic high-wavenumber internal waves in the Kuroshio. *J. Phys. Oceanogr.*, **36**, 1104–1122.
- Ramp, S. R., T.-Y. Tang, T. F. Duda, J. F. Lynch, A. K. Liu, C.-S. Chiu, F. L. Bahr, H.-R. Kim and Y.-J. Yang (2004): Internal solitons in the northeastern South China Sea Part I: sources and deep water propagation. *IEEE J. Oceanic Eng.*, **29**(4), 1157–1181.
- Tian, J., Q. Yang, X. Liang, L. Xie, D. Hu, F. Wang and T. Qu (2006): Observation of Luzon Strait transport. *Geophys. Res. Lett.*, **33**, L19607, doi:10.1029/2006GL026272.
- Toole, J. M., R. W. Schmitt and K. L. Polzin (1994): Estimates of diapycnal mixing in the abyssal Ocean. *Science*, **264**(5162), 1120–1132, DOI: 10.1126.
- Yanagi, T. and T. Takao (1998): A numerical simulation of tides and tidal currents in the South China Sea. *Acta Oceanogr. Taiwan.*, **37**(1), 17–29.
- Yang, Y. J., T.-Y. Tang, M.-H. Chang, A. K. Liu, M.-K. Hsu and S. R. Ramp (2004): Solitons northeast of Tung-Sha Island during the ASIAEX pilot studies. *IEEE J. Oceanic Eng.*, **29**, 1182–1199.
- Zhao, Z. and M. H. Alford (2006): Source and propagation of internal solitary waves in the northeastern South China Sea. *J. Geophys. Res.*, **111**, C11012, doi:10.1029/2006JC003644.